The Astrophysical Journal, 821:107 (10pp), 2016 April 20 doi:10.3847/0004-637X/821/2/107

THE ROLL-OVER OF HELIOSPHERIC NEUTRAL HYDROGEN BELOW 100 eV: OBSERVATIONS AND IMPLICATIONS

A. Galli[1], P. Wurz[1], N. A. Schwadron[2], H. Kucharek[2], E. Möbius[2], M. Bzowski[3], J. M. Sokół[3], M. A. Kubiak[3], H. O. Funsten[4], S. A. Fuselier[5,6], and D. J. McComas[5,6]
[1] Physics Institute, University of Bern, Bern, 3012, Switzerland
[2] University of New Hampshire, Durham, NH 03824, USA
[3] Space Research Centre, Polish Academy of Sciences, Warsaw, 00-716, Poland
[4] Los Alamos National Laboratory, Intelligence and Space Research Division, Los Alamos, NM 87545, USA
[5] Southwest Research Institute, San Antonio, TX 78228, USA
[6] University of Texas, San Antonio, TX 78249, USA
Received 2016 January 25; accepted 2016 March 3; published 2016 April 19

ABSTRACT

We present an improved analysis of the energy spectrum of energetic neutral hydrogen from the heliosheath observed with the *IBEX*-Lo sensor on the *Interstellar Boundary EXplorer* from the years 2009 to 2012. This analysis allows us to study the lowest energies between 10 and 100 eV although various background sources are more intense than the targeted signal over broad areas of the sky. The results improve our knowledge of the interaction region between our heliosphere and the interstellar plasma because these neutral atoms are direct messengers from the low-energy plasma in the heliosheath. We find a roll-over of the energy spectrum below 100 eV, which has major implications for the pressure balance of the plasma in the inner heliosheath. The results can also be compared directly with in situ observations of the *Voyager 1* and *2* spacecraft.

Key words: ISM: general – plasmas – solar wind – Sun: heliosphere

1. INTRODUCTION

The *Interstellar Boundary Explorer* (*IBEX*) has been observing the interaction of the heliosphere with the surrounding interstellar medium since 2009 January (McComas et al. 2009). The scientific payload consists of two sensors, *IBEX*-Lo (Fuselier et al. 2009) and *IBEX*-Hi (Funsten et al. 2009). This study presents the energy spectra of heliospheric energetic neutral atoms (ENAs) from various directions in the sky observed with *IBEX*-Lo. *IBEX*-Lo measures ENAs in eight overlapping energy bins from 2 keV down to 0.01 keV. This range translates into ENAs from solar wind energy down to energies of neutral hydrogen atoms from the cold heliosheath. These energy spectra improve our knowledge of the inner heliosheath, i.e., the plasma region beyond the termination shock of the heliosphere where the solar wind is slowed down to subsonic speed. The results can also be compared to independent in situ (the *Voyager 1* and *2* spacecraft) and remote measurements (Lyα absorption lines of nearby stars).

In Section 2 we present the data set and how we reconstructed ENA spectra with the corresponding uncertainties from *IBEX*-Lo observations. Section 3 summarizes the results of the spectra, Section 4 discusses the implications of our results for our knowledge of the heliosphere, and Section 5 concludes the paper.

2. DATA SET

We rely on the method presented by Galli et al. (2014) to create maps of differential intensities of heliospheric hydrogen ENAs at a heliocentric distance of 100 au in the inertial reference frame with respect to the Sun. The observations cover the time from 2009 January until 2012 June and all eight energy bins of the *IBEX*-Lo sensor with the central energies at 0.015, 0.029, 0.055, 0.11, 0.209, 0.439, 0.872, and 1.821 keV (Fuselier et al. 2009). The intensities were corrected for the energy-dependent survival probability of ENAs (see Appendix B in McComas et al. 2014) and for the proper motion of the spacecraft relative to the Sun. Throughout this study, we will refer to the frame transformation as "Compton–Getting correction." We applied a Compton–Getting correction to the data for a piecewise power-law spectrum between two neighboring energy bins. The fitted power-law parameter was free to vary with energy and direction and also could become positive, indicating a roll-over. We assumed the energy of neutral hydrogen ENAs at their place of origin in the heliosheath to be equal to their energy at a heliocentric distance of 1 au. The observation time from 2009 until 2012 roughly coincides with the solar minimum, and for these conditions the energy loss of ENAs due to solar radiation pressure is nearly compensated by the energy gain due to solar gravity (Bzowski 2008). The relevant ENA energies therefore correspond to the nominal center values for energy bins 1 to 8 in *IBEX*-Lo.

Since the publication by Galli et al. (2014), we have improved our evaluation method in four ways. First, the calculation of ENA survival probabilities has been updated based on a new assessment of ionization rates in the years 2009 to 2012 (see the Appendix). The ubiquitous background and its uncertainty below 0.2 keV (*IBEX*-Lo energy bins 1 to 4) have been updated based on the work presented in Galli et al. (2015). The more conservative definition for the regions affected by the inflow of interstellar neutrals (ISN) has been applied (Galli et al. 2014), resulting in the exclusion of more pixels. Finally, we have accepted observation times only if the TOF2 count rate of *IBEX*-Lo did not exceed 1.6 times the average rate. This approach is routinely used for background suppression in ISN studies (Möbius et al. 2012, 2015; Galli et al. 2015). This additional requirement selectively excludes observations affected by a high electron background, which is an indication of contamination due to Earth's magnetosphere or the solar wind. As a result, the average ENA signal and its upper limit of

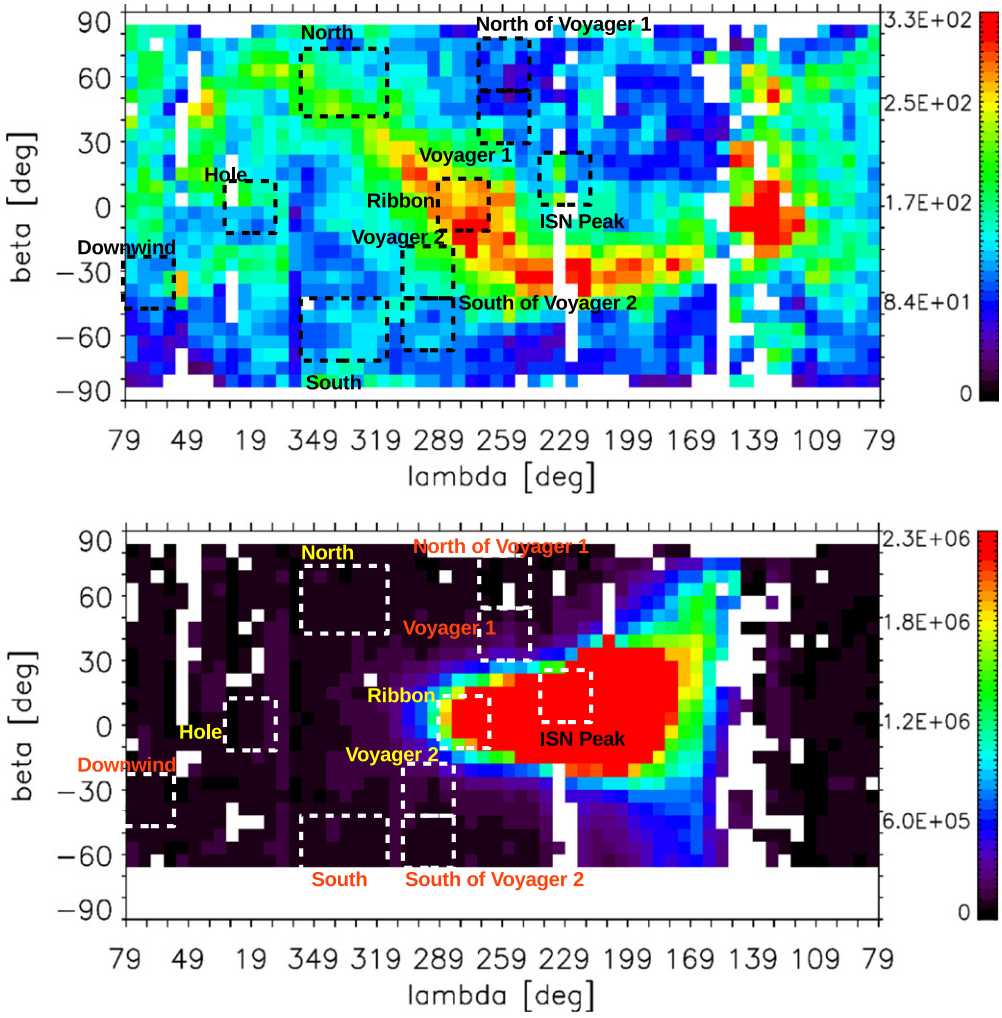

Figure 1. Maps of measured ENA intensities in energy bin 7 (top panel, 0.8 keV central energy) and energy bin 1 (bottom panel, 0.015 keV central energy), averaged from 2009 January to 2012 June. The dashed squares indicate the regions where energy spectra were sampled. Whereas at 0.8 keV most of the ENAs are due to heliospheric ENAs, the intense signal at the lowest energy is due to interstellar neutral helium, which is excluded from this study.

uncertainty tend to be lower than in Galli et al. (2014) because outliers due to local contaminations are more efficiently excluded.

The observation times for this study include the first four years of *IBEX* observations, i.e., the eight half-year maps from 2009 January until 2012 June. Later data were not considered because they have a lower signal-to-noise ratio: the post-acceleration of *IBEX*-Lo had to be reduced in 2012 July and the background caused by the terrestrial magnetosphere and the solar wind increased in later years as the solar cycle neared its maximum (Galli et al. 2015). From the eight half-year maps we synthesized energy spectra, averaged over the entire time, for several sky regions for all eight energy bins of *IBEX*-Lo. The sky regions were chosen in such a manner as to coincide with the regions defined in previous publications (Fuselier et al. 2012, 2014; Galli et al. 2014) and to include as many pixels as possible that are not strongly contaminated by Earth's magnetosphere nor by the ISN inflow. The above requirements allowed us to define 10 regions: Downwind, Hole, North, South, *Voyager 2* and the adjacent region to the south, Ribbon, *Voyager 1* and the adjacent region to the north, and ISN Peak. These regions are indicated in the map in ecliptic coordinates in Figure 1 and listed in Table 1. The maps are centered at $\lambda = 259°$ to be in accordance with ENA maps in previous *IBEX* publications (Galli et al. 2014; McComas et al. 2014). The 10 regions can be divided into two groups. The upwind hemisphere includes the six regions that lie within $\pm 90°$ ecliptic longitude to the upwind direction at $\lambda_\infty = 255.°7$ (McComas et al. 2015). As can be seen in the lower panel of Figure 1, the maximum ISN signal is shifted with respect to that direction by roughly 30° because of the curved trajectories of neutral helium in the solar system (Möbius et al. 2012). The combination of the four remaining regions (Downwind, North, South, ENA Hole) will be referred to as the "downwind hemisphere." The *Voyager 1* and *Voyager 2* directions are of special interest because of the available in situ observations by the *Voyager* spacecraft (Decker et al. 2005; Fisk & Gloeckler 2013; Gurnett et al. 2013; Krimigis et al. 2013; Stone et al. 2013). The regions adjacent to the *Voyager 1* and *2* directions were added to check for a potential ISN contamination in the *Voyager 1* and *Voyager 2* regions at the lowest energy (see the lower panel in Figure 1).

The upper panel of Figure 1 shows the ENA intensities in energy bin 7 (0.872 keV) corrected for survival probability and for Compton–Getting effects. The lower panel shows measured intensities in energy bin 1 (0.015 keV) without application of

Table 1
Map Regions Used in this Study and the Various Sources of Contamination

Name	λ_{ecl}	β_{ecl}	Non-heliospheric Contributions
Downwind	55°...79°	−48°...−24°	Magnetosphere, ubiquitous background
ENA Hole	7°...31°	−12°...+12°	Magnetosphere, ubiquitous background
North	313°...355°	+42°...+72°	Ubiquitous background
South	313°...355°	−72°...−42°	Ubiquitous background
Voyager 2	283°...307°	−42°...−18°	ISN?, ubiquitous background
South of *Voyager 2*	283°...307°	−66°...−42°	Ubiquitous background
ENA Ribbon	265°...289°	−12°...+12°	ISN, ubiquitous background
Voyager 1	247°...271°	+30°...+54°	ISN?, ubiquitous background
North of *Voyager 1*	247°...271°	+54°...+78°	Ubiquitous background
ISN Peak	217°...241°	0°...+24°	ISN, ubiquitous background

Note. The regions are defined as rectangular regions in ecliptic longitude and latitude (λ_{ecl}, β_{ecl}). Refer to Figure 1 for a map.

any correction. Two background sources are apparent in Figure 1. The bright stripe of high ENA intensities between 79° and 160° longitude in the upper panel is caused by Earth's magnetosphere. The bright triangular shape around 229° longitude in the lower panel is due to the inflow of ISN helium. It consists of the main peak near the ecliptic plane plus a spatially extended population of helium around it, the so-called "Warm Breeze" (Kubiak et al. 2014, 2016; Sokół et al. 2015). The interstellar helium creates a signal of apparent hydrogen ENAs in *IBEX*-Lo as the helium atoms sputter hydrogen atoms off the conversion surface of the instrument. The resulting signal is up to three orders of magnitude more intense than the signal due to heliospheric hydrogen ENAs in energy bins 1 to 3 below 0.1 keV (Galli et al. 2014). For this study, the ISN signal—both the main peak and the Warm Breeze—is considered to be a contamination and is excluded following the more conservative of the approaches studied by Galli et al. (2014). As a result, most pixels at energies below 0.1 keV obtained in the upwind hemisphere had to be rejected.

The sky regions are of equal size, 4 × 4 pixels, with one pixel covering 6° in ecliptic longitude and latitude, which is close to the instantaneous *IBEX*-Lo field of view of 6.°5 × 6.°5 (Fuselier et al. 2009). The only exception to this rule are the two larger regions labeled "North" and "South." They include all pixels that are not affected by the intense signal of ISN at low energies and for which both ram and antiram observations are available. These regions were crucial to quantify the ubiquitous background described by Galli et al. (2014): the strength of the heliospheric ENA signal at a distance of 100 au from the Sun must not depend on the proper motion of the spacecraft. Therefore, we could quantify the background to be subtracted from the total signal before Compton–Getting correction by demanding that the intensity of true heliospheric ENAs in the inertial reference frame must be the same for ram and for antiram observations. Because of the relative velocity between ENAs and the spacecraft, observations along the ecliptic plane would be most sensitive to the Compton–Getting correction and thus to the presence of the local background. This region had to be avoided for this study due to the intense signal of ISNs. But the effect of ram versus antiram observations is still very relevant at the latitudes covered by the North and South regions. The agreement of energy spectra obtained during ram and antiram observations for those regions will be an important test for the validity of our approach (see Section 3).

The energy spectrum entry at a given energy bin is the median value of ENA intensities of all single pixels within the region taken from all seasonal maps individually. We verified that no significant spatial variability occurred within a single region and that no significant change with time occurred in any of the eight regions. For the latter verification, we compared the averages and standard deviations of the ENA intensities from the years 2009 and 2010 with those from 2011 and 2012 for each energy bin. Out of 54 different cases where a standard deviation for each pair of years could be derived, only three averages deviated by more than two standard deviations from each other between earlier and later years. For the North, South, and the *Voyager 1* and *Voyager 2* regions, we also verified that the standard deviation over single pixels did not increase when we combined all four years instead of combining only the earlier two and the latter two years in a data set. This also holds true if only ram observations are considered. This test demonstrates that we do not enlarge the error spread by averaging energy spectra over four years. Relying on *IBEX*-Hi ENA maps with a better signal-to-noise ratio, McComas et al. (2012) found a general trend of decreasing ENA intensities with time. The intensity ratio, averaged over all ram pixels measured in 2011 and 2009, yielded $j_{2011}/j_{2009} = 0.89$, 0.78, 0.85 for *IBEX*-Hi energies 0.7, 1.1, and 1.7 keV. We find $j_{2011}/j_{2009} = 0.8$, 0.8, 0.9 and $j_{2012}/j_{2009} = 1.2$, 1.1, 1.0 for the average over all ram pixels in *IBEX*-Lo maps at the energy bins centered at the *IBEX*-Lo energies 0.439, 0.872, and 1.821 keV. The error bars of the intensity ratios derived from *IBEX*-Lo are typically 0.3, i.e., as large as or larger than the temporal change expected from *IBEX*-Hi observations.

The uncertainty of the ENA intensity derived for a single map pixel depends on both statistical and systematic errors. For the purposes of this study, the first type of error can be neglected. The statistical error is due to the fact that only a few counts are registered in a single pixel per season (one half-year map). The lowest count rates in *IBEX*-Lo due to heliospheric ENA are usually registered in energy bin 5 (Galli et al. 2014). At this energy, the total signal amounts to typically seven counts per season per pixel, four of which are due to background. In the absence of any additional background (such as magnetospheric contamination), the total signal and the background would follow Poisson distributions, with the standard deviation equal to the square root of the expectation value. Since we average over at least 16 pixels to obtain the regional ENA intensity per season, and most regions considered in this study were covered in at least four different seasons, the relative statistical uncertainty of the ENA intensity

after background subtraction is thus calculated to be

$$\frac{\sigma_{\rm ENA}}{j_{\rm ENA}} \leqslant \frac{\sqrt{7 \times 4 \times 16 + 4 \times 4 \times 16}}{(7-4) \times 4 \times 16} \approx 0.14. \quad (1)$$

Given systematic relative errors of 50%, this uncertainty introduced by count statistics is negligible.

We studied two different approaches to quantify the systematic errors that translate into an error estimate of a spectral entry. We chose the variability of the single pixels observed within a region and during the consecutive seasons as the default error estimate. To be more robust against outliers we used the median and a lower and a higher quantile, comprising 16% and 84% of all values, as results. These quantiles are chosen in such a way that they equal the normal standard deviation measure if the values in a region are normally distributed. We compared these uncertainties to the expectations from the error propagation analysis performed in our previous study (see Figure 5 in Galli et al. 2014). Since that analysis, the uncertainties of the throughput correction and of the ubiquitous background have been updated. This has only minor effects on the relative uncertainties at lower energy bins. The new array of relative uncertainties for a heliospheric ENA signal for energy bins 1 to 8 reads: 62%, 57%, 50%, 45%, 45%, 45%, 37%, and 32%. This agrees well with the estimate by Fuselier et al. (2012), who used 30% relative uncertainty for energy bins 5 to 8, and 50% relative uncertainty for the four lower energy bins. For energies where most single-pixel intensities are significantly larger than zero, the variability agrees with the error propagation approach. For instance, the relative uncertainties of median ENA intensities in the region "North" estimated from the spread between the 16% and 84% quantiles reach 72%, 53%, 39%, and 28% for energy bins 5 to 8. However, the error propagation approach breaks down when the ENA intensities after background subtraction come close to zero because the error propagation function becomes discontinuous.

3. RESULTS

We first verified that the reconstructed ENA energy spectrum in the inertial reference frame does not change between ram and antiram observations of the same sky region. Otherwise, subtracting the ubiquitous background (Galli et al. 2014, 2015) was insufficient to exclude all local sources (local to the spacecraft or to the Earth) from the data before we applied the Compton–Getting correction. As mentioned in Section 2, we have only the two regions "North" and "South" that were observed in both configurations. Figure 2 shows that the energy spectra from ram and antiram observations are indistinguishable within the error bars. The error bars are the spread between the 16% and 84% quantiles as a proxy for the total uncertainty. This comparison also illustrates that the error bars for antiram observations are always higher than for ram observations because of the worse signal-to-noise ratio. At energy bins 3 (0.055 keV) and 4 (0.11 keV), the error bars might be too conservative since the four values are much closer to each other than the span of the error bars. For the two lowest energy bins, on the other hand, the median ENA intensity can be any value between zero (no symbols plotted) and 5000 $\rm cm^{-2}\,sr^{-1}\,s^{-1}\,keV^{-1}$. The ENA intensities around 1 keV energy are higher in the North than in the South because of the ENA Ribbon (see upper panel in Figure 1).

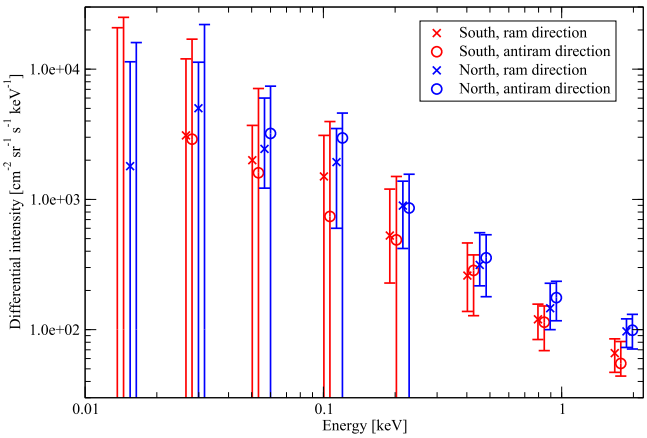

Figure 2. Energy spectra of heliospheric ENA intensity in the inertial reference frame at a heliocentric distance of 100 au. This figure shows the two different regions in the downwind hemisphere (South and North), for which independent ram and antiram observations are available. Error bars represent the spatial and temporal variability, derived as 16% and 84% quantiles. Error bars with no symbols indicate that the ENA signal is not significantly higher than the background and give the upper limit. The spectral entries were evaluated at the identical energy among the four different data sets; the symbols in the plot are shifted slightly to enhance legibility.

In the following, a heliospheric ENA intensity of zero means that the measured signal is not significantly higher than the ubiquitous background at low energies. Approximating the ubiquitous background as 0.01 cnts $\rm s^{-1}$ and using 1 count = 0.0015 cnts $\rm s^{-1}$ (Galli et al. 2015), we expect 7×16 counts per season and region if there is no heliospheric ENA signal beside the background. The observed number of counts would in principle follow a Poissonian, which can be approximated by a normal distribution as the expectation value is much larger than 1. A simple statistical test would thus be to count the fraction of cases of median count rates larger than the background count rates, i.e., cases with a positive median ENA intensity after background subtraction. If this fraction is significantly larger than 50% the hypothesis that there is no heliospheric ENA intensity beside the background must be excluded. Unfortunately, magnetospheric contamination and other non-constant background sources will add positive outliers, potentially leading to false positives. In addition, these background sources usually affect several adjacent pixels per orbit. We therefore must not consider single pixels from the same season as statistically independent. We will count instead how many seasonal median values are larger than zero after background subtraction. With a signal consisting solely of a constant background that is normally distributed the probability of finding a median larger than that background in m out of N seasons is

$$p = 0.5^N \binom{N}{m}. \quad (2)$$

If we combine the four regions in the downwind hemisphere, we find that 6/21 (6 out of 21), 10/21, 16/21, 17/21, and 21/21 median values are larger than zero for energy bins 1 to 5, respectively. The probabilities that these fractions of m/N are obtained by chance without an additional signal are calculated via Equation (2) as $p = 0.96$, 0.5, 0.01, 0.004, and 5×10^{-7}. The observations in the two lowest energy bins ($E < 0.05$ keV) are consistent with the hypothesis that there is no ENA signal beside the background. For higher energies, this hypothesis can

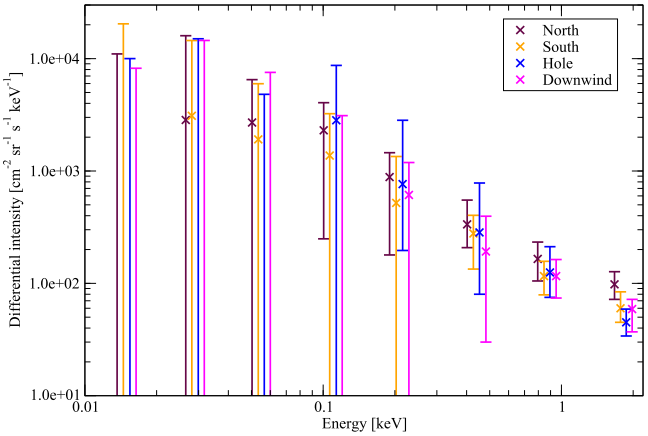

Figure 3. Energy spectra of heliospheric ENA intensity in the inertial reference frame at at a heliocentric distance of 100 au for the four different regions in the downwind hemisphere—South (including ram and antiram observations), North (including ram and antiram observations), Hole, and Downwind. Same format as Figure 2.

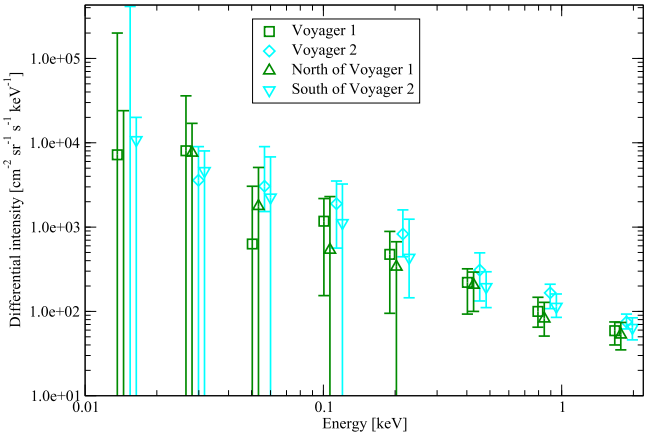

Figure 4. Energy spectra of heliospheric ENA intensity in the inertial reference frame at a heliocentric distance of 100 au for *Voyager 1* and the region north of it (green squares and green triangles) and for *Voyager 2* and the neighboring region south of it (cyan diamonds and triangles). Same format as Figure 2.

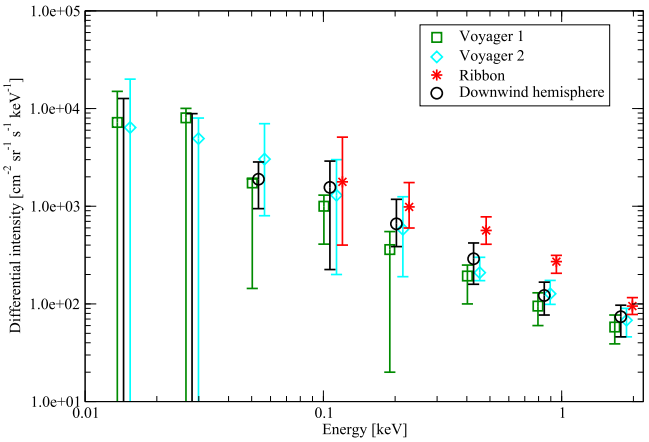

Figure 5. The four best constrained energy spectra of heliospheric ENA intensity in the inertial reference frame at a heliocentric distance of 100 au: downwind hemisphere (black symbols), *Voyager 1* plus adjacent region (green squares), *Voyager 2* plus adjacent region (cyan diamonds), and the Ribbon direction (red asterisks). The error bars indicate that in the two lowest energy bins the ENA signal is not significantly higher than the background. Same format as Figure 2.

be rejected with 95% confidence. The median ENA intensity in the lowest energy bin amounts to zero with an upper limit of typically $10^4\,\mathrm{cm^{-2}\,sr^{-1}\,s^{-1}\,keV^{-1}}$ in all four regions of the downwind hemisphere (see Figure 3). The *Voyager 1* direction was covered in only two seasons at the lowest energy with a sufficient signal-to-noise ratio. To make a statistical statement we had to combine the *Voyager 1* region with its adjacent region to the north, which is covered in four consecutive years during ram observations. As for the downwind hemisphere, we also find for *Voyager 1* and *Voyager 2* directions that the heliospheric ENA signal is significant (95%) against the background only for energy bin 3 and higher energies. In the subsequent spectral plots, error bars of combined spectra will reflect the likelihood that a true heliospheric ENA signal exists. For energies of 0.05 keV or higher, the lower limit will be the lowest positive median value instead of zero, even if the 16% quantile happens to be zero.

The spectra for the four different regions in the downwind hemisphere are shown in Figure 3, whereas Figure 4 shows the four regions around *Voyager 1* and *2* directions in the upwind hemisphere. These spectra represent the globally distributed heliospheric ENA signal and the overlying Ribbon signal (Schwadron et al. 2014) at a distance of 100 au. In both figures, the values represent median values over all single pixels from all observation seasons; the error bars are the 16% and 84% quantiles of the single-pixel values. The four ENA spectra from the downwind hemisphere are indistinguishable below 1 keV (see Figure 3); the higher intensity at 1.87 keV in the North region is due to the Ribbon at high latitudes. In the upwind hemisphere, the intensities measured in the *Voyager 2* direction tend to be higher than those from the *Voyager 1* direction for all energies above 0.05 keV. The spectral entries for *Voyager 1* and *2* directions are identical with those from their adjacent regions within the error bars.

In this study we are mainly interested in the globally distributed heliospheric ENA signal at low energies. We therefore created a combined "downwind hemisphere" spectrum (see Figure 5) from the four individual downwind regions as the median value over the 21 individual seasonal and regional median values. Averaging the four downwind spectra shown in Figure 3 yields an energy spectrum identical to that shown in Figure 5 within the error bars. For the lowest energy, both approaches yield zero, i.e., no discernible heliospheric ENA signal above the background. The error bars are the 16% and 84% quantiles of the 21 median values or the global error bars from error propagation, whichever are larger. The merging of several regions of course hides the differences at high energies due to the ENA Ribbon, but it allows us to reduce the uncertainties at low energies. Most of the upwind hemisphere is inaccessible to this study at low energies, because the inflow of ISN is orders of magnitude more intense than the heliospheric ENA signal below 0.4 keV (Galli et al. 2014). Moreover, the region $79^\circ \leqslant \lambda_{\mathrm{ecl}} \leqslant 160^\circ$ is strongly contaminated by background from Earth's magnetosphere (see the vertical stripe of red and green pixels in Figure 1). Therefore, the *Voyager 1* and *Voyager 2* directions and the adjacent pixels toward the poles are the only regions where we can follow the heliospheric ENA signal down to the lowest energy bin in the upwind hemisphere. Similar to the combined Downwind spectrum, the combined *Voyager 1* and *Voyager 2* spectra in Figure 5 are

Table 2
Energy Spectra of Heliospheric ENA Intensities in Units of cm^{-2} sr^{-1} s^{-1} keV^{-1} as Shown in Figure 5

Energy	Downwind Hemisphere	*Voyager 1*	*Voyager 2*	Ribbon
	Hemisphere			
0.015 keV	0^{+13000}_{-0}	7200^{+7800}_{-7200}	6400^{+13600}_{-6400}	N/A
0.029 keV	0^{+9000}_{-0}	8000^{+2000}_{-8000}	4900^{+3100}_{-4900}	N/A
0.055 keV	1900^{+900}_{-900}	1730^{+170}_{-1590}	3000^{+4000}_{-2200}	N/A
0.110 keV	1600^{+1300}_{-1300}	1000^{+300}_{-590}	1300^{+1710}_{-1100}	1800^{+3300}_{-1400}
0.209 keV	660^{+520}_{-280}	360^{+190}_{-340}	580^{+670}_{-390}	980^{+760}_{-390}
0.439 keV	290^{+130}_{-130}	193^{+57}_{-93}	209^{+91}_{-36}	570^{+210}_{-160}
0.872 keV	122^{+45}_{-45}	95^{+35}_{-35}	127^{+47}_{-28}	271^{+43}_{-65}
1.821 keV	74^{+23}_{-28}	58^{+19}_{-19}	68^{+22}_{-22}	95^{+21}_{-17}

Note. Downwind hemisphere: average of South, North, Hole, and Downwind; *Voyager 1*: $+30° \leqslant \beta_{ecl} \leqslant +78°$, $247° \leqslant \lambda_{ecl} \leqslant 271°$; *Voyager 2*: $-66° \leqslant \beta_{ecl} \leqslant -18°$, $283° \leqslant \lambda_{ecl} \leqslant 307°$; Ribbon: $-12° \leqslant \beta_{ecl} \leqslant +12°$, $265° \leqslant \lambda_{ecl} \leqslant 289°$.

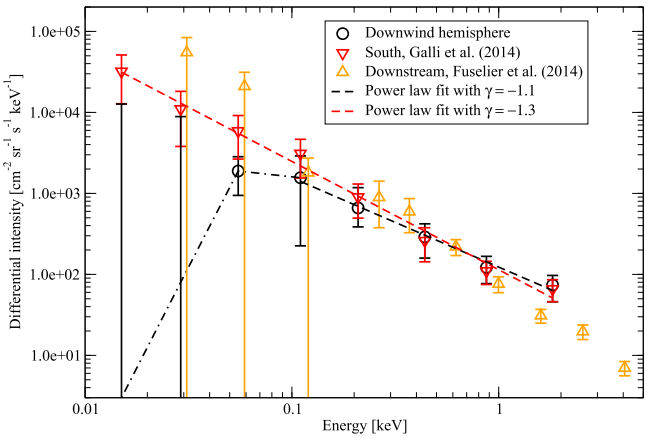

Figure 6. Energy spectra of heliospheric ENAs in the downwind hemisphere derived in this study (black symbols) vs. ENA energy spectra published by Galli et al. (2014) (red triangles down) and Fuselier et al. (2014) (orange triangles up) for similar regions. The black line shows the power law with $\gamma = -1.1$, which describes well the observations at energies above 0.1 keV. For lower energies, the old energy spectrum was consistent with a uniform power law continuing to the lowest energies (red dashed line); the present study indicates that the energy spectrum more likely bends over and disappears at low energies (black dashed–dotted line).

the median values from all individual seasons covered in *Voyager 1* and *2* directions plus their respective adjacent regions toward the poles (see Figure 1 and Table 1).

Figure 5 shows the combined downwind hemisphere spectrum (black symbols) including all four downwind regions, "*Voyager 1*" (green squares) including *Voyager 1* and its adjacent region, and "*Voyager 2*" including the *Voyager 2* direction and its adjacent region (cyan diamonds). The advantage of these combined spectra over the single regions in Figures 3 and 4 is the broader coverage at the lowest energies for *Voyager 1* and *Voyager 2* directions, which would be covered in only one or two seasons without the additional regions. Moreover, the likelihood analysis allowed us to decide which intensities are significantly larger than zero. The energy spectrum of the Ribbon region is denoted with red asterisks in Figure 5. Below 0.1 keV, heliospheric ENAs from the Ribbon direction cannot be observed due to the contamination of the ISN. The values shown in Figure 5 are listed in Table 2.

The energy spectrum of any direction where we have valid measurements at the lowest energies (Downwind, *Voyager 1*, and *Voyager 2*) becomes flatter below 0.1 keV, and none of those energy spectra show a significant signal above the background in the two lowest energy bins (see Figure 5). This implies that no hydrogen ENAs (within the upper limit derived from our analysis) are produced with energies below ~40 eV in the plasma beyond the termination shock and directed back into the heliosphere. Between 0.1 and 1.8 keV, 6 out of 10 spectra can be described by a power law with slope -1.2 ± 0.1. The energy spectrum at the ENA Hole is significantly steeper, $\gamma = -1.6 \pm 0.2$, and the Hole disappears at energies below 0.5 keV. The spectrum at the Ribbon region is flatter, $\gamma = -1.0 \pm 0.1$, because of the additional ENAs at solar wind energies. The Ribbon in our designated region vanishes between 0.2 and 0.1 keV, consistent with previous studies by Fuselier et al. (2009, 2012), Schwadron et al. (2014), and Galli et al. (2014). At 0.1 keV, the Ribbon spectrum does not exceed the globally distributed ENA signal observed from other regions in the sky (see Figure 5). The two regions close to the poles show a flatter spectrum. For instance, $\gamma = -0.9 \pm 0.1$ for the *Voyager 1* North region compared to $\gamma = -1.1 \pm 0.1$ for the *Voyager 1* region at lower latitudes. The trend of intensities at *Voyager 2* being higher than at *Voyager 1* by about 30% continues down to 0.05 keV. In the two lowest energy bins, the median ENA intensity around the *Voyager 1* direction exceeds that in the *Voyager 2* direction and in the downwind hemisphere, but the difference is not significant given the error bars. For the same reason, we cannot prove that the heliospheric spectrum differs between upwind and downwind regions.

Figure 6 compares the combined Downwind spectrum from this study (black circles) with the "South" spectrum published earlier by Galli et al. (2014) (red triangles down) and with the "Downstream" spectrum by Fuselier et al. (2014) (orange triangles up). Above 0.1 keV all three spectra agree with each other. The discrepancies at lower energies can be understood if we look at the different definitions of regions and at the differences in method. The "South" region as defined by Galli et al. (2014) is not identical to our current definition. It was centered around 295° longitude and thus lay closer to the Ribbon and the ISN inflow. The energy spectra from Galli et al. (2014) in the hemisphere of the ISN inflow were probably contaminated by the sputtering signal from the spatially extended Warm Breeze. The second reason for the lower ENA intensities at low energies in the new analysis is the more rigorous data selection that includes the TOF2 count rate (see Section 2). The changes of survival probabilities and background levels had little effect on the resulting ENA intensities. Fuselier et al. (2014) combined *IBEX*-Lo and *IBEX*-Hi measurements from the "Downstream" direction, averaging over the four map pixels around $\lambda = 72°$, $\beta = -36°$. The reason for the higher upper limits given by Fuselier et al. (2014) at low energies is the treatment of the ubiquitous background. Fuselier et al. (2014) did not subtract it and interpreted their results at low energies as upper limits of the heliospheric signal. In Galli et al. (2014) and the present study, we explicitly subtracted this background from the measured signal, which led to a substantial reduction in the heliospheric ENA intensities. The dashed black line in Figure 6 is a power law with an exponent $\gamma = -1.1$ fitted to the new Downwind

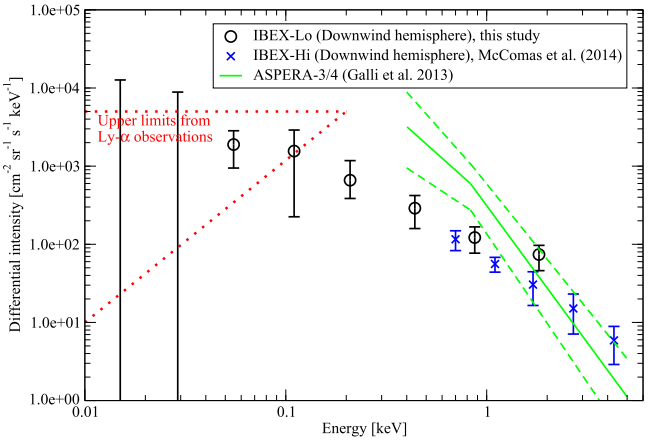

Figure 7. Comparison of heliospheric ENA spectra from the available space observations at energies below 5 keV. Black symbols: *IBEX*-Lo, average downwind hemisphere (this study), blue symbols: *IBEX*-Hi, South region (McComas et al. 2014), green curves: ASPERA-3&4, globally averaged spectrum plus its 1σ uncertainties (Galli et al. 2013). The red dotted lines denote upper limits derived from independent Lyα observations (Wood & Izmodenov 2010; Fuselier et al. 2014).

data points between 0.1 and 1.8 keV. The dashed–dotted line is a line to guide the eye based on the new energy spectrum below 0.1 keV. From the new results based on the more rigorous data selection, it is very improbable that the three spectral points obtained at 0.015, 0.029, and 0.055 keV follow the power law established at higher energies. This probability, $p = 0.002$, is determined by the product of the three deviations between the extrapolated power-law line and the actual values divided by the respective standard deviation. The energy spectrum of heliospheric neutral hydrogen in Figure 6 very likely rolls over at 0.1 keV. For the *Voyager 1* and *Voyager 2* regions (see Figure 5), a continuous power law cannot be ruled out. The uncertainty of ENA intensities at low energies is simply too large because of the limited number of uncontaminated regions in the upwind hemisphere.

Figure 7 shows a compilation of measured heliospheric ENA spectra at energies below 5 keV and the upper limits from independent Lyα observations (Wood et al. 2007; Wood & Izmodenov 2010). Symbols in black denote the Downwind energy spectrum from this study (taken from Figure 6). The symbols in blue denote *IBEX*-Hi results for the South region (McComas et al. 2014) (Data Release 7, five-year averages from 2009–2013 of ram maps, corrected for Compton–Getting effect and survival probability). The relative uncertainty attributed to *IBEX*-Hi measurements is 20% (Fuselier et al. 2012) or the standard deviation between the four different regions, whichever is larger. The green curve represents the global average of heliospheric ENAs measured with ASPERA-3&4 on board *Mars Express* and *Venus Express* (Galli et al. 2013). This globally averaged spectrum does not differ within the error bars from the spectrum one would obtain if only observations from the downwind hemisphere are included. The dashed lines indicate the lower and upper 1σ error bar. The ASPERA-3&4 ENA spectra were measured during the cruise phases to Mars and Venus in the years 2003–2006 at heliocentric distances ranging from 0.7 to 1.5 au. This means that the 1 keV ENAs observed with ASPERA-3&4 had originated in the heliosheath during solar maximum conditions, whereas ENAs of that energy observed during the first years of the *IBEX* mission were produced in solar minimum conditions. The ENA sensor of ASPERA-3&4 has many strongly overlapping TOF bins, which means that one usually can fit enough parameters to define a peak or a two-component power law. The energy range of ASPERA-3&4 observations (0.4–5.0 keV) was too narrow to confirm the roll-over at 0.1 keV observed with *IBEX*-Lo. On the other hand, the ASPERA-3&4 observations provide an independent experimental confirmation that the steepening of the spectral slope at the energy overlap between *IBEX*-Lo and *IBEX*-Hi around 1 keV (Fuselier et al. 2012) is a physical reality and not an artifact. In ASPERA-3&4 data, which have a higher energy resolution than *IBEX*, this knee was found to reside at 0.83 ± 0.12 keV (Galli et al. 2013). The only discrepancy between the *IBEX* and the ASPERA-3&4 observations is the steeper spectral slope of the latter. This discrepancy could be due to the different observation time and viewing directions or due to an incomplete knowledge of the energy dependence of the sensor efficiencies.

As discussed by Fuselier et al. (2014), Lyα observations of absorption lines from nearby stars (Wood et al. 2007; Wood & Izmodenov 2010) impose upper limits on neutral hydrogen atoms in the heliosphere at energies below 0.2 keV. The Lyα observations referred to by Fuselier et al. (2014) are Lyα spectra measured with the *Hubble Space Telescope* for various lines of sight through the heliosphere. These Lyα observations generally fail to detect any absorption from heliospheric ENAs at low energy, with the exception of a few weak detections very near the downwind direction toward the heliotail (Wood et al. 2007, 2014). This upper limit from Lyα observations was another reason—the main reason being that the derived ENA intensities depended on spacecraft position—why Fuselier et al. (2014) concluded that the measured ENA energy spectrum below 0.1 keV had to be contaminated by a local background. The new *IBEX*-Lo energy spectra at low energies are consistent with the upper limits derived from Lyα observations (red dotted lines in Figure 6). Two different lines are shown for the upper limit because the spectral shape is unknown (Fuselier et al. 2014). The upper limit from Lyα observations is most restrictive in the downwind direction; ENA intensities up to 10^4 cm^{-2} sr^{-1} s^{-1} keV^{-1} along the *Voyager 1* direction (see Figure 5) are not ruled out by Lyα observations.

4. IMPLICATIONS FOR THE HELIOSPHERE

The updated energy spectra of heliospheric ENAs at low energies have several implications for our understanding of the heliosphere and the ion populations in the heliosheath.

Desai et al. (2014) assumed heliospheric ENA intensities of several thousand cm^{-2} sr^{-1} s^{-1} keV^{-1} at 0.1 keV in the *Voyager 1* and *Voyager 2* directions based on earlier analyses of *IBEX*-Lo measurements (Fuselier et al. 2012, 2014; Galli et al. 2014). Models including only ENA sources in the inner heliosheath (Gloeckler & Fisk 2010; Zank et al. 2010) predict an intensity ~1000 cm^{-2} sr^{-1} s^{-1} keV^{-1} at this energy. Desai et al. (2014) therefore concluded that an additional source of ENAs from the outer heliosheath—the region of perturbed interstellar plasma beyond the heliopause (Heerikhuisen et al. 2014; Zirnstein et al. 2014)—was likely necessary to explain the ENA energy spectrum observed below 0.5 keV. The authors suggested that "a significant fraction of the low-energy ENAs between ~0.1 and 0.5 keV observed by *IBEX* could be created by a non-thermalized hotter, pickup-ion population" in the outer heliosheath. For ENAs above 0.5 keV,

Table 3
Stationary and Dynamic Plasma Pressure in the Inner Heliosheath.

Energy	Stationary Pressure times line of sight (pdyn cm^{-2} au)		Correction Factor		Dynamic Pressure times line of sight (pdyn cm^{-2} au)	
	Downwind	*Voyager 1*	Downwind	*Voyager 1*	Downwind	*Voyager 1*
0.015 keV	$0^{+0.8}_{-0}$	$0.4^{+0.4}_{-0.4}$	437.2	14.4	0^{+350}_{-0}	$5.8^{+5.8}_{-5.8}$
0.029 keV	$0^{+1.8}_{-0}$	$1.6^{+0.4}_{-1.6}$	156.5	7.6	0^{+282}_{-0}	$12.2^{+3.1}_{-12.2}$
0.055 keV	$1.1^{+0.5}_{-0.5}$	$1.0^{+0.1}_{-0.9}$	62.3	4.6	$68.5^{+31.1}_{-31.1}$	$4.6^{+0.5}_{-4.1}$
0.110 keV	$3.0^{+2.4}_{-2.4}$	$1.9^{+0.6}_{-1.1}$	25.7	3.0	$77.1^{+61.7}_{-61.7}$	$5.7^{+1.8}_{-3.3}$
0.209 keV	$3.6^{+2.8}_{-1.5}$	$2.0^{+1.1}_{-1.9}$	12.6	2.2	$45.4^{+35.3}_{-18.9}$	$4.4^{+2.3}_{-4.2}$
0.439 keV	$5.7^{+2.5}_{-2.5}$	$3.6^{+1.1}_{-1.7}$	6.4	1.8	$36.5^{+16.0}_{-16.0}$	$6.5^{+2.0}_{-3.1}$
0.872 keV	$7.8^{+2.9}_{-2.9}$	$6.1^{+2.2}_{-2.2}$	3.9	1.5	$30.4^{+11.3}_{-11.3}$	$9.2^{+3.3}_{-3.3}$
1.821 keV	$17.6^{+5.5}_{-6.7}$	$13.8^{+4.5}_{-4.5}$	2.6	1.3	$45.8^{+14.3}_{-17.4}$	$17.9^{+5.8}_{-5.8}$

Note. Results are derived from the ENA energy spectrum for the downwind hemisphere and for the *Voyager 1* direction. The dynamic pressure is the stationary pressure times the velocity-dependent correction factor (see Equation (3)).

on the other hand, Desai et al. (2014) also assumed an origin from solar wind and pickup ions in the inner heliosheath. The new energy spectra presented here in Figure 5 indicate an ENA intensity of only 1000–2000 cm^{-2} sr^{-1} s^{-1} keV^{-1} at 0.1 keV. Thus, a smaller contribution from hot pickup ions in the outer heliosheath would be sufficient to explain the observations. The new results (note the uncertainty of energy spectra in Figure 5 around 0.1 keV) are also consistent with no ENAs below 0.5 keV originating from the outer heliosheath.

According to the model by Gloeckler & Fisk (2015), heliospheric ENAs below 0.05 keV must originate from the cold high-density solar wind in the heliosheath, ENAs of intermediate energies from 0.05 to 0.5 keV are produced by hot high-density solar wind, whereas ENAs of higher energies originate from pickup protons. These three components suffice to reproduce the globally distributed ENA fluxes from previous publications of *IBEX*-Lo and *IBEX*-Hi data (Fuselier et al. 2012). ENA sources from the outer heliosheath are not required. Our new energy spectra are consistent with this model. The most notable addendum concerns the three lowest energy bins: in the downwind hemisphere no contribution from cold high-density solar wind is needed, whereas this component seems to be required for the *Voyager 1* direction and, to a lesser extent, for the *Voyager 2* direction (see Figure 5). From Gloeckler & Fisk (2015) we would expect a non-zero ENA signal in the *Voyager 1* direction in the lowest energy bin but very low or zero ENA signals for most other sky directions. We emphasize, however, that neither the observed median ENA intensity in the *Voyager 1* direction nor that in the *Voyager 2* direction is significantly higher than the background at energies below 0.05 keV.

We repeated the plasma pressure calculation presented by Schwadron et al. (2011) and Fuselier et al. (2012) for the new ENA energy spectrum. The results for the downwind hemisphere and for the *Voyager 1* region are summarized in Table 3. The measured intensity $j_{\rm ENA}$ of neutralized hydrogen at a given energy translates into a pressure of the parent ion population in the heliosheath times the integration length along the line of sight, $\Delta P \times l$, in the following way:

$$\Delta P \times l = \frac{4\pi}{3 n_{\rm H}} m_{\rm H} v \frac{j_{\rm ENA}(E)}{\sigma(E)} \Delta E \; c_f \qquad (3)$$

$$c_f = \frac{(v + u_R)^2}{v^4}(v^2 + 4u_R^2 + 2u_R v). \qquad (4)$$

In Equation (3), ΔE denotes the width of the respective energy bin; for the typical radial velocity of solar wind in the flanks and the downwind hemisphere of the inner heliosheath, we assumed $u_R = 140$ km s^{-1} as measured by *Voyager 2*, whereas $u_R = 40$ km s^{-1} for the heliosheath in the *Voyager 1* direction (Schwadron et al. 2011; Gloeckler & Fisk 2015). For the density of neutral hydrogen in the inner heliosheath a constant $n_{\rm H} = 0.1$ cm^{-3} is assumed (Schwadron et al. 2011; Gloeckler & Fisk 2015). The charge-exchange cross section between protons and neutral hydrogen decreases from (4 to 2) $\times$ 10^{-15} cm^{-2} for 0.015 to 1.821 keV (Lindsay & Stebbings 2005). The integration length l for ENA production in the plasma is approximately the thickness of the inner heliosheath. The part of Equation (3) without the velocity factor c_f can be interpreted as stationary pressure. The total pressure or dynamic pressure is the stationary pressure times this factor. Integrating over all energy bins in Table 3, we obtain the total plasma pressure times heliosheath thickness as $P \times l = 304$ pdyn cm^{-2} au for the downwind hemisphere and 66 pdyn cm^{-2} au for the *Voyager 1* region (1 pdyn cm^{-2} au = 0.015 N m^{-1}). If we want to put these numbers into the context of other studies, we face two problems. First, the uncertainty of the total pressure is large given the upper limits in the two lowest energy bins. Second, heliosheath plasma more energetic than 2 keV will produce ENAs that cannot be detected with *IBEX*-Lo. We therefore used the observed median $j = 0$ cm^{-2} sr^{-1} s^{-1} keV^{-1} for heliospheric ENAs in the two lowest energy bins of *IBEX*-Lo and relied on the study by Livadiotis et al. (2013). They compared the expected plasma pressure from a kappa distribution of protons with the plasma pressure derived from *IBEX*-Hi energy spectra: the energy range between 0.03 and 2 keV, roughly corresponding to the *IBEX*-Lo range, covered more than half of the total plasma pressure predicted from a kappa distribution. The authors found a total plasma pressure of $P = 2.1$ pdyn cm^{-2} for all sky directions except for the ENA Ribbon. Gloeckler & Fisk (2015) presented a multi-component plasma model for the heliosheath

to explain *Voyager* and *IBEX* observations. At low energies they assumed the ENA energy spectra provided by Fuselier et al. (2012). They derived a total pressure of 2.5 pdyn cm^{-2} in all three plasma regions in the nose of the heliotail (Gloeckler & Fisk 2015). Pressure contributions from the slowed solar wind, magnetic pressure, and the pressure exerted from pickup ions and anomalous cosmic rays all had to be taken into account to obtain this total pressure.

The ENA spectra measured in the *Voyager 1* direction yield similar stationary pressures as the Downwind spectra, as can be seen from Figure 5. But because of a much lower radial velocity of the plasma, $u_R = 40\,km\,s^{-1}$ (Gloeckler & Fisk 2015), the dynamic pressure times the heliosheath thickness is much smaller. In the direction of *Voyager 1*, the heliosheath thickness is roughly $l = 50$ au (Gloeckler & Fisk 2015), whereas no in situ observations exist for the downwind hemisphere. The new analysis of *IBEX*-Lo spectra yields $P = 1.4\,pdyn\,cm^{-2}$ for the integral plasma pressure in the *Voyager 1* direction. As expected from Livadiotis et al. (2013) this is smaller than but close to the theoretical plasma pressure of 2.1 pdyn cm^{-2}. Keeping in mind that the measured energy spectrum in the downwind hemisphere is similar to that observed in the *Voyager 1* region, we can therefore estimate the typical thickness of the heliosheath in the downwind hemisphere to be $l = P \times l/1.4 = 220 \pm 110$ au. This estimate cannot be more accurate than 50% because of the pressure contributions from energies above 2 keV and because of the uncertainties of the derived plasma pressures in Table 3. Along the heliotail (the "Downwind" region in Figure 1) the radial velocity u_R and $P \times l$ will likely be larger, resulting in a wider heliosheath. The stationary component of the pressure is similar in all examined regions of the downwind hemisphere (see Figure 3).

Due to the improved analysis of low-energy ENA measurements, the derived dynamic pressure does not continually increase with decreasing energies below 0.2 keV. The roll-over in ENA energy spectra results in the dynamic pressure leveling off around 50 eV. If the power law observed at solar wind energies were to continue all the way down to thermal energies the total plasma pressure would reach infinity and the heliosphere would become unstable. This is a fundamental argument for the existence of a roll-over in the ENA energy spectrum.

5. CONCLUSIONS

We have compiled energy spectra of heliospheric ENAs from *IBEX*-Lo measurements in 2009–2012 down to energies of 0.01 keV, representing the best available data set of ENA energy spectra at these low energies so far.

As noted in previous studies, the ENA Ribbon is most apparent at solar wind energies (1 keV) and vanishes around 0.1 keV. At lower energies, the energy spectrum of the globally distributed ENA signal looks the same for all viewing directions in the sky within the respective error bars. The spectrum of heliospheric ENAs very likely (confidence >95%) starts to roll over at 0.1 keV in the downwind hemisphere. The presence of heliospheric ENAs is not evident for energies below 0.05 keV in any viewing direction. The energy spectra below 0.5 keV can be explained without the addition of ENAs originating from the outer heliosheath. The ENA intensities from the *Voyager 2* direction are higher than those from *Voyager 1* for all energies between 0.05 and 2 keV. In the two lowest energy bins, the ENA signal strength from the *Voyager 1* direction seems to exceed the intensities from the downwind hemisphere and from the *Voyager 2* direction. This is consistent with the presence of cold high-density solar wind in the nose region of the heliosphere. However, the differences in measured energy spectra are not significant because of the large uncertainties introduced by local background sources.

The energy spectra measured with *IBEX*-Lo are compatible with the upper limit set by Lyα observations of stellar absorption lines. The total plasma pressure in the inner heliosheath integrated over the energy range of *IBEX*-Lo measurements comes close to the ~2 pdyn cm^{-2} expected for a parameterized kappa distribution of protons. This plasma pressure implies an inner heliosheath thickness of a few hundred au in the downwind hemisphere, given the thickness of 50 au in the nose direction measured with *Voyager 1*.

In the coming years, the solar activity will decrease again with an expected solar minimum around 2020. This decrease will result in a lower background in *IBEX*-Lo data and thus will offer the opportunity for additional observations of low-energy ENAs at a favorable signal-to-noise ratio.

We thank all of the outstanding men and women who have made the *IBEX* mission such a wonderful success. A.G. and P.W. thank the Swiss National Science foundation for financial support. M.B., M.A.K., and J.M.S. were supported by Polish National Science Center grant 2012-06-M-ST9-00455. H.K., E.M., N.S., H.O.F., S.A.F., and D.J.M. were supported by the NASA Explorer program as a part of the *IBEX* mission.

APPENDIX

The improved survival probabilities of hydrogen ENAs are calculated using the method presented in Appendices B in McComas et al. (2012, 2014), based on updated information on the relevant solar factors. Hydrogen is ionized by charge exchange with solar wind protons, photoionization by the solar EUV flux, and electron impact ionization due to solar wind electrons. Hydrogen atoms are also subjected to a repulsive force of the solar radiation in the Lyα line (Bzowski et al. 2013). The solar Lyα flux used to calculate the radiation pressure and also the photoionization rate have been updated following an update recently introduced to the composite Lyα series released by the Laboratory for Atmospheric and Space Physics (Woods et al. 1996, 2000). These changes resulted in a small upward change of a few per cent in the composite flux, thus slightly increasing the photoionization rate. These changes are smaller than the uncertainty of the model and are of a secondary importance for the total hydrogen ionization rate. In the meantime, the solar wind model (Sokół et al. 2013) was also updated with the most current available data sets: the in-ecliptic data sets from the NASA project Operating Missions as a Node on the Internet, updated and revised based on historical records, and the newest observations of interplanetary scintillation used to determine the heliolatitudinal structure of the solar wind speed and density. For the newest set of survival probabilities we used the spin-axis pointing determined by Swaczyna et al. (2015). All these small updates resulted in the new time series of survival probabilities illustrated in Figure 8. The upper panel shows the spectrum of survival probabilities for the eight energy bins of *IBEX*-Lo for different sky directions (see Table 1 for the complete set of regions; a map is presented in Figure 1). The lower panel of Figure 8 shows the relative change of the survival probabilities with respect to

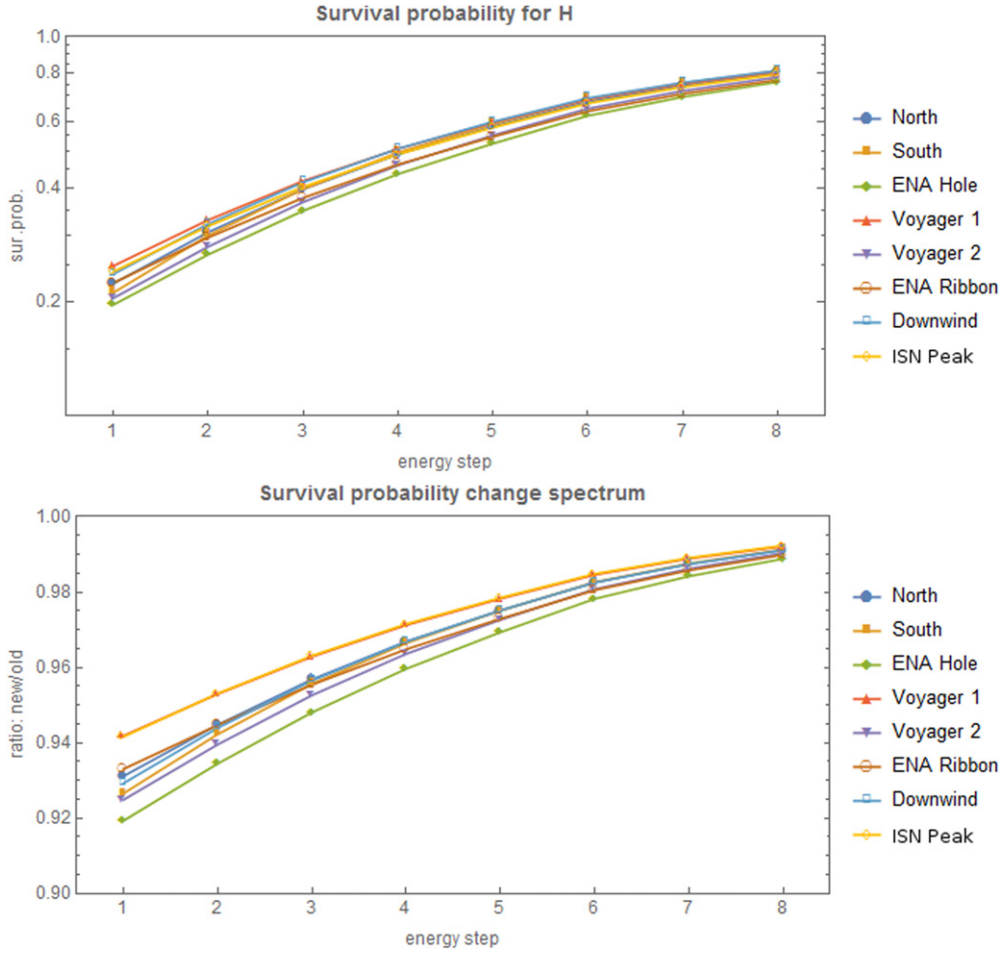

Figure 8. Updated survival probabilities used for this study. The upper panel shows energy spectra of survival probabilities averaged over the sky regions defined in Table 1 for the first four years of *IBEX* observations in the ram direction. A survival probability of 1.0 implies no losses of hydrogen ENAs from a heliocentric distance of 100 au to the instrument at 1 au. The lower panel shows the relative changes of these survival probabilities compared to the previous values.

those we used previously. The modifications are less than 10% for the energy range covered by *IBEX*-Lo. The largest changes are for the region in the energy space where the roll-over of the hydrogen ENA spectrum is expected.

REFERENCES

Bzowski, M. 2008, A&A, 488, 1057
Bzowski, M., Sokół, J. M., Kubiak, M. A., & Kucharek, H. 2013, A&A, 557, A50
Decker, R. B., Krimigis, S. M., Roelof, E. C., et al. 2005, Sci, 309, 2020
Desai, M. I., Allegrini, F., Bzowski, M., et al. 2014, ApJ, 780, 98
Fisk, L. A., & Gloeckler, G. 2013, ApJ, 776, 79
Funsten, H. O., Allegrini, F., Bochsler, P., et al. 2009, SSRv, 146, 75
Fuselier, S. A., Allegrini, F., Bzowski, M., et al. 2012, ApJ, 754, 14
Fuselier, S. A., Allegrini, F., Bzowski, M., et al. 2014, ApJ, 784, 89
Fuselier, S. A., Bochsler, P., Chornay, D., et al. 2009, SSRv, 146, 117
Galli, A., Wurz, P., Fuselier, S. A., et al. 2014, ApJ, 796, 9
Galli, A., Wurz, P., Kollmann, P., et al. 2013, ApJ, 775, 24
Galli, A., Wurz, P., Park, J., et al. 2015, ApJS, 220, 30
Gloeckler, G., & Fisk, L. A. 2010, in AIP Conf. Proc. 1302, Pickup Ions Throughout the Heliosphere and Beyond, ed. J. A. Le Roux, G. P. Zank, A. J. Coates, & V. Florinski (Melville, NY: AIP), 110
Gloeckler, G., & Fisk, L. A. 2015, ApJL, 806, L27
Gurnett, D. A., Kurth, W. S., Burlaga, L. F., & Ness, N. F. 2013, Sci, 341, 1489
Heerikhuisen, J., Zirnstein, E. J., Funsten, H. O., Pogorelov, N. V., & Zank, G. P. 2014, ApJ, 784, 73
Krimigis, S. M., Decker, R. M., Roelof, E. C., et al. 2013, Sci, 341, 144
Kubiak, M. A., Bzowski, M., Sokół, J. M., et al. 2014, ApJS, 213, 29
Kubiak, M. A., Swaczyna, P., Bzowski, M., et al. 2016, ApJ, in press
Lindsay, B. G., & Stebbings, R. F. 2005, JGR, 110, A12213
Livadiotis, G., McComas, D. J., Schwadron, N. A., Funsten, H. O., & Fuselier, S. A. 2013, ApJ, 762, 134
McComas, D. J., Allegrini, F., Bochsler, P., et al. 2009, SSRv, 146, 11
McComas, D. J., Allegrini, F., Bzowski, M., et al. 2014, ApJS, 213, 20
McComas, D. J., Bzowski, M., Fuselier, S. A., et al. 2015, ApJS, 220, 22
McComas, D. J., Dayeh, M. A., Allegrini, F., et al. 2012, ApJS, 203, 1
McComas, D. J., Dayeh, M. A., Funsten, H. O., Livadiotis, G., & Schwadron, N. A. 2013, ApJ, 771, 77
Möbius, E., Bochsler, P., Bzowski, M., et al. 2012, ApJS, 198, 11
Möbius, E., Bzowski, M., Fuselier, S. A., et al. 2015, JPhCS, 577, 012019
Schwadron, N. A., Allegrini, F., Bzowski, M., et al. 2011, ApJ, 731, 56
Schwadron, N. A., Möbius, E., Fuselier, S. A., et al. 2014, ApJ, 215, 13
Sokół, J. M., Bzowski, M., Tokumaru, M., Fujiki, K., & McComas, D. J. 2013, SoPh, 285, 167
Sokół, J. M., Bzowski, M., Kubiak, M. A., et al. 2015, ApJS, 220, 29
Stone, E. C., Cummings, A. C., McDonald, F. B., et al. 2013, Sci., 341, 15
Swaczyna, P., Bzowski, M., Kubiak, M. A., et al. 2015, ApJS, 220, 26
Wood, B. E., & Izmodenov, V. V. 2010, in AIP Conf. Proc. 1302, Pickup Ions Throughout the Heliosphere and Beyond, ed. J. le Roux et al. (Melville, NY: AIP), 18
Wood, B. E., Izmodenov, V. V., Alexashov, D. B., Redfield, S., & Edelman, E. 2014, ApJ, 780, 108
Wood, B. E., Izmodenov, V. V., Linsky, J. L., & Malama, Y. G. 2007, ApJ, 657, 609
Woods, T. N., Prinz, D. K., Rottman, G. J., et al. 1996, JGR, 101, 9541
Woods, T. N., Tobiska, W. K., Rottman, G. J., & Worden, J. R. 2000, JGR, 105, 27195
Zank, G. P., Heerikhuisen, J., Pogorelov, N. V., Burrows, R., & McComas, D. J. 2010, ApJ, 708, 1092
Zirnstein, E. J., Heerikhuisen, J., Zank, G. P., et al. 2014, ApJ, 783, 129